

Article

A Ka-Band Integrated Six-Port Chip for Analog Complex Correlator

Wangdong He, Xi Chen , Jianhao Gong, Anyong Hu * and Jungang Miao

School of Electronics and Information Engineering, Beihang University, Beijing 100191, China; hwd19930315@buaa.edu.cn (W.H.); chenxi0913@buaa.edu.cn (X.C.); gongjh@buaa.edu.cn (J.G.); jmiaobremen@buaa.edu.cn (J.M.)

* Correspondence: hu_anyong@buaa.edu.cn; Tel.: +86-138-1142-1892

Abstract: Six-port technology has been widely used in microwave systems, such as interferometric passive imaging. In this paper, an integrated Ka-band (32–36 GHz) six-port chip based on the 0.15- μm GaAs technology is designed and fabricated to simplify the circuit structure and miniaturize the volume of the imaging system. The designed chip integrates two amplifiers, two phase shifters, and a six-port circuit as part of an analog complex correlator. In this integrated chip, the crosstalk between the two amplifiers cannot be ignored. This paper analyzes the influence of the isolation between two amplifiers on the correlation results to guide the six-port chip design. In addition, considering that the radiometer system receives a broadband noise signal, the phase shifter needs to ensure that the phase shift range of each frequency point is the same under the same control conditions. Therefore, the phase shifter is designed with a high-pass and low-pass structure. The measurement results show that the isolation between the two amplifiers is greater than 20 dB, and the measured phase shift range and phase shift range error of the designed chip are 220° and 10° , respectively, with the control voltage varying from 0 to 1.5 V, which meets the requirements of the system.

Keywords: interferometric passive imaging; analog complex correlator; six-port technology; amplifier; phase shifter



Citation: He, W.; Chen, X.; Gong, J.; Hu, A.; Miao, J. A Ka-Band Integrated Six-Port Chip for Analog Complex Correlator. *Sensors* **2022**, *22*, 4877. <https://doi.org/10.3390/s22134877>

Academic Editor: Simone Genovesi

Received: 11 May 2022

Accepted: 22 June 2022

Published: 28 June 2022

Publisher's Note: MDPI stays neutral with regard to jurisdictional claims in published maps and institutional affiliations.



Copyright: © 2022 by the authors. Licensee MDPI, Basel, Switzerland. This article is an open access article distributed under the terms and conditions of the Creative Commons Attribution (CC BY) license (<https://creativecommons.org/licenses/by/4.0/>).

1. Introduction

The basic work related to six-port technology was carried out in the 1970s, primarily by Engen and Hoer [1–4]. Since that time, six-port technology has developed rapidly and has been widely used in many fields, such as reflectometer [5,6], radar detection [7–10], antenna measurement [11,12], and interferometric passive imaging [13].

In the application of interferometric passive imaging, the correlator is the key component. Both analog and digital approaches can be applied to correlators. The digital correlator has the advantages of high stability and flexible configuration [14,15]. The analog correlator has the benefits of large continuum bandwidth, high sensitivity, low costs, and low power consumption [16–19]. Furthermore, the analog correlator is followed by a relatively simple data acquisition and processing subsystem.

The analog correlator can be implemented using either direct multiplication technology [18–21] or add-and-square technology [22,23]. The direct multiplication analog correlator is normally carried out using non-linear devices such as mixers or analog multipliers [24]. Due to the limitation of multiplier chips, the correlator has the disadvantage of low bandwidth and operates in the low-frequency range. The add-and-square analog correlator can achieve wide bandwidth and high sensitivity at the expense of larger volume and complex structure [25–27], and it is normally based on six-port technology [28]. In addition, the add-and-square analog complex correlator can obtain the amplitude and phase information of the two input signals by measuring the correlation of received signals. In order to obtain the complete correlation circle, the phase difference between the two input signals needs to be swept from 0° to 360° .

A six-port network, which has two inputs and four outputs, is a passive microwave system composed of couplers and power dividers [29–31]. The six-port network can be realized by microstrip technology [32–35], but it leads to the six-port being larger and inhibits the miniaturization of the correlator. Therefore, in order to increase the integration of the system, a six-port network fabricated on the chip, which may integrate other circuits, such as a detector or amplifier, has been reported in recent years [36–40]. The chip integration improves the accuracy and reduces the size of the six-port circuit.

In the application of interferometric millimeter-wave passive imaging, the higher input frequency means better spatial resolution, which is very important to the system [41,42]. In addition, the temperature sensitivity of a radiometer is inversely proportional to the square root of the system bandwidth [43]. The interferometric imaging system can easily obtain larger bandwidth at a higher frequency, thereby increasing the temperature sensitivity of the system. In the design of interferometric imaging systems, the receiver front-end works in the high-frequency range (such as the Ka-band), but its correlator works in a lower frequency band (such as C-band, 4–8 GHz) [15,44–46]. Therefore, a local oscillator (LO) chain is introduced into the system to down-convert the received radio frequency (RF) signal to obtain the intermediate frequency (IF) signal with a lower frequency. A simple block diagram of the interferometric imaging system is represented in Figure 1.

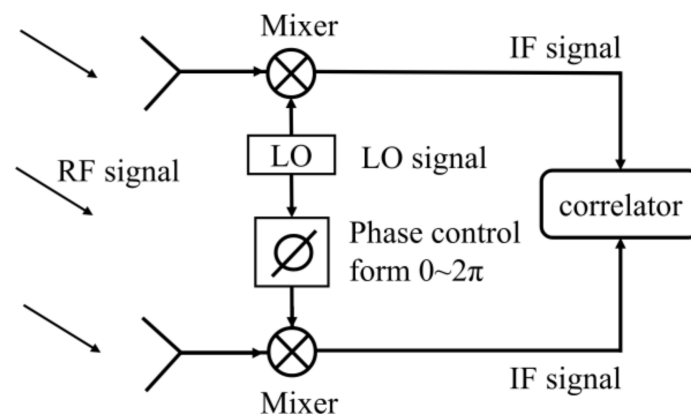


Figure 1. A simple block diagram of the interferometric imaging system.

It is worth noting that the phase control module is designed in the LO chain, which is used to change the phase difference between two input RF signals from 0° to 360° to obtain a complete correlation circle in the correlator. However, this method adds an additional LO link and increases the complexity of the system. Especially for the passive millimeter-wave imaging system with a large number of receiver channels, it needs the same number of LO signals, and the LO chain is a burden to the system that cannot be ignored.

In this article, a Ka-band integrated six-port chip is designed and fabricated based on $0.15\text{-}\mu\text{m}$ GaAs pHEMT technology. The designed chip integrates two amplifiers, two phase shifters, and a six-port circuit as part of an analog complex correlator, and it is used for interferometric passive millimeter-wave imaging applications [47]. The block diagram of the proposed integrated six-port chip is represented in Figure 2. In this structure, two amplifiers at two input ports are used to provide gain to the input RF signals, which can compensate for the signal loss caused by the phase shifter and six-port network. The phase shifter is a phase control module to change the phase of input RF signals, and the six-port network comprised of a power divider and 3-dB hybrid couplers is used to shift the signal phases and addition of the input signals. The theory of the complex cross-correlation circuits is described, and the influence of the isolation between two amplifiers on the correlation results is analyzed to guide the integrated six-port chip design. The phase shifter with low-pass and high-pass structure is simulated and designed, which has the characteristics of broadband phase-shifting compared with the phase shifter with only

low-pass structure. Based on the designed integrated six-port chip, the measurement isolation between two amplifiers and phase shift range is performed and analyzed.

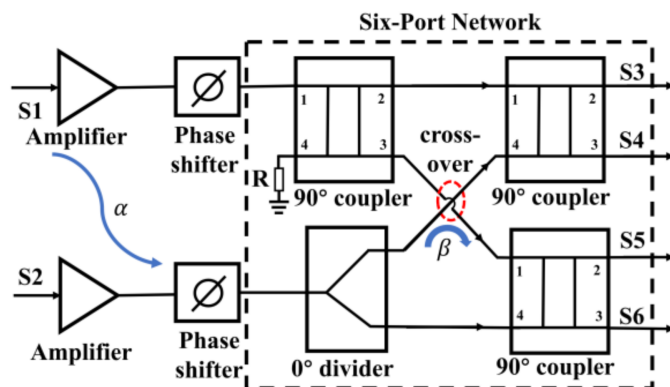


Figure 2. The block diagram of the proposed six-port chip integrated with two amplifiers, two phase shifters, and a six-port circuit.

The remainder of this article is structured as follows. In Section 2, we describe the theory of the complex cross-correlation circuits, after which the influence of the isolation between two amplifiers is given to guide the six-port circuit design. Section 3 presents the design of the integrated six-port chip, including the design of each single function circuit and the simulation of the whole integrated circuit. In Section 4, the measurement results employing the integrated six-port chip are presented. The conclusion is provided in Section 5.

2. Analysis of the Analog Complex Correlator Based on the Integrated Six-Port Chip

In the interferometric passive imaging system, an ideal analog complex cross-correlator is usually used to measure the phase difference between two input signals. The six-port cross-correlator can obtain the phase difference by first adding and then squaring the two input signals. In our team's previous work [28,45], the analog complex cross-correlator based on the six-port technology, shown in Figure 3, was applied in a passive imaging system for security applications. It can be seen that the six-port network consists of a power divider and three couplers.

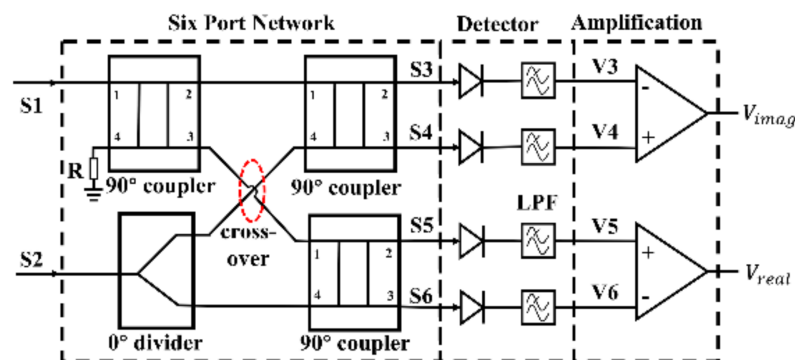


Figure 3. Topology of the complex cross-correlator circuit based on six-port technology.

2.1. Theory of the Analog Complex Correlator

This section introduces the theory of the analog complex correlation circuits in an ideal case. Assuming the inputs are two single-frequency signals $S_1(t)$ and $S_2(t)$, which can be presented as:

$$\begin{aligned} S_1(t) &= \cos(\omega_0 t + \theta_1) \\ S_2(t) &= \cos(\omega_0 t + \theta_2) \end{aligned} \tag{1}$$

Then, the four output signals of the six-port network can be described as:

$$\begin{aligned} S_3 &= S_1 + \hat{S}_2 = \cos(\omega_0 t + \theta_1) + \sin(\omega_0 t + \theta_2) \\ S_4 &= \hat{S}_1 + S_2 = \sin(\omega_0 t + \theta_1) + \cos(\omega_0 t + \theta_2) \\ S_5 &= \hat{S}_1 + \hat{S}_2 = \sin(\omega_0 t + \theta_1) + \sin(\omega_0 t + \theta_2) \\ S_6 &= -S_1 + S_2 = -\cos(\omega_0 t + \theta_1) + \cos(\omega_0 t + \theta_2) \end{aligned} \quad (2)$$

where \hat{S}_1 is Hilbert transform of S_1 , which is used to represent the phase of signal shifted by 90° in the six-port signal distribution network.

The following detector circuits with the square-law characteristic and low pass filter (LPF) transform input signals (S_3 – S_6) to useful output dc voltages (V_3 – V_6). After the differential amplification circuits, the real and imaginary parts of the cross-correlation function can be obtained [28] as:

$$\begin{aligned} V_{real} &= GV_{2nd} \cos(\theta_1 - \theta_2) \\ V_{imag} &= GV_{2nd} \sin(\theta_1 - \theta_2) \end{aligned} \quad (3)$$

where G is the gain of the differential amplification circuit, and V_{2nd} is the dc voltage resulting from the second-order transconductance of the square-law detector. In order to characterize the performance of the correlator, a correlation circle has been formed through the real and imaginary parts of the correlation results. In addition, the broadband characteristic of the correlator can be evaluated by using the correlation circles.

2.2. Influence of Isolation between Two Amplifiers on Correlation Results

In this article, the fabricated integrated six-port chip contains amplification, phase-shifting, and signal distribution circuits, as shown in Figure 2. Since these circuits are implemented on a chip with a small size, the effect of signal coupling on the correlation results has to be considered. In this section, the isolation between two amplifiers at the input port is mainly considered. Moreover, we can analyze the influence of the isolation between two amplifiers on the correlation results under the condition that other components of the correlator are ideal.

Assuming that the voltage coupling coefficient between two amplifiers is α , and it varies from 0 to 1. The two inputs are still single-frequency signals $S_1(t)$ and $S_2(t)$, then two input signals of six ports can be described as:

$$\begin{aligned} S'_1 &= \sqrt{1 - \alpha^2} S_1 + \alpha S_2 \\ S'_2 &= \alpha S_1 + \sqrt{1 - \alpha^2} S_2 \end{aligned} \quad (4)$$

In this condition, the four output signals of the six-port network can be described as:

$$\begin{aligned} S'_3 &= \sqrt{1 - \alpha^2} (S_1 + \hat{S}_2) + \alpha (\hat{S}_1 + S_2) \\ S'_4 &= \sqrt{1 - \alpha^2} (\hat{S}_1 + S_2) + \alpha (S_1 + \hat{S}_2) \\ S'_5 &= \sqrt{1 - \alpha^2} (\hat{S}_1 + \hat{S}_2) + \alpha (\hat{S}_1 + \hat{S}_2) \\ S'_6 &= \sqrt{1 - \alpha^2} (-S_1 + S_2) + \alpha (S_1 - S_2) \end{aligned} \quad (5)$$

After the zero-biased square-law detector and LPF, the useful output dc voltage can be expressed as:

$$\begin{aligned} V'_3 &= \frac{V_{2nd}}{2} \left[1 - (1 - 2\alpha^2) \sin(\theta_1 - \theta_2) + 2\alpha \sqrt{1 - \alpha^2} \cos(\theta_1 - \theta_2) \right] \\ V'_4 &= \frac{V_{2nd}}{2} \left[1 + (1 - 2\alpha^2) \sin(\theta_1 - \theta_2) + 2\alpha \sqrt{1 - \alpha^2} \cos(\theta_1 - \theta_2) \right] \\ V'_5 &= \frac{V_{2nd}}{2} \left[(1 + 2\alpha \sqrt{1 - \alpha^2}) \times (1 + \cos(\theta_1 - \theta_2)) \right] \\ V'_6 &= \frac{V_{2nd}}{2} \left[(1 - 2\alpha \sqrt{1 - \alpha^2}) \times (1 - \cos(\theta_1 - \theta_2)) \right] \end{aligned} \quad (6)$$

Then, the real and imaginary parts of the cross-correlation function can be obtained as

$$\begin{aligned} V_{real} &= GV_{2nd} \left[2\alpha\sqrt{1-\alpha^2} + \cos(\theta_1 - \theta_2) \right] \\ V_{imag} &= GV_{2nd} (1 - 2\alpha^2) \sin(\theta_1 - \theta_2) \end{aligned} \quad (7)$$

Compared to the ideal case, it can be seen that the isolation between two input amplifiers has an influence on the amplitude of the imaginary part of the cross-correlation function and adds a dc offset error to the real part of the cross-correlation function. In addition, the relationship between isolation (*ISO*) and voltage coupling coefficient α can be expressed as:

$$ISO = -20 \log(\alpha) \quad (8)$$

According to Equations (7) and (8), the variation of the correlation circle with the isolation can be obtained, and then the radius of the correlation circle can be fitted according to the least square method, and the result is shown in Figure 4.

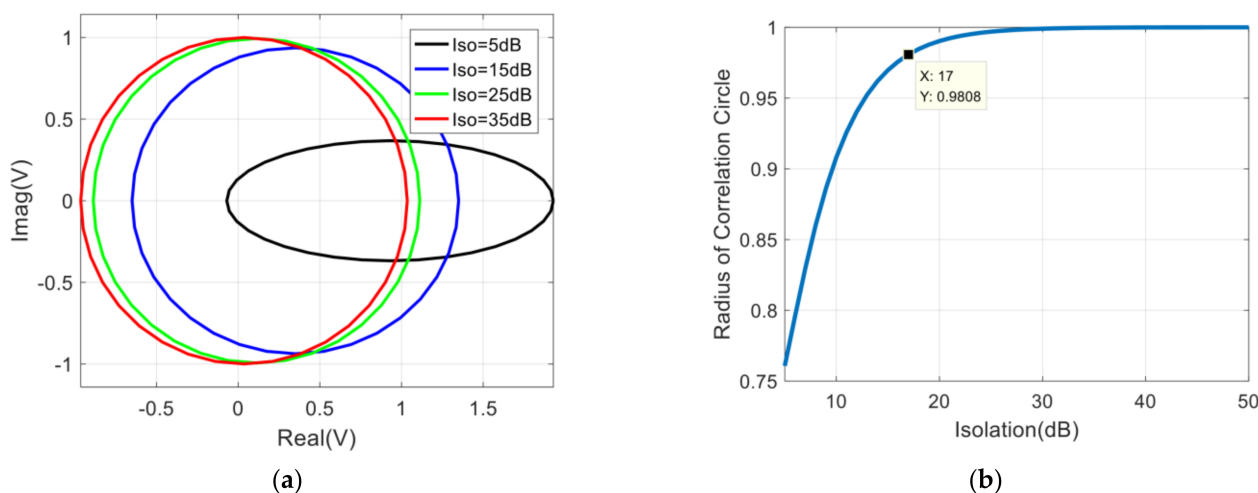


Figure 4. Influence of isolation between two amplifiers on correlation results: (a) The variation of the correlation circle with the isolation; (b) The variation of the radius of the correlation circle with the isolation.

Since the dc offset error does not vary with the phase difference of the input signal ($\Delta\theta = \theta_1 - \theta_2$), it can be calibrated by using the measurement results of the correlator by changing $\Delta\theta$ in the range of 2π at equal intervals [46]. Generally speaking, the correlation coefficient of the analog correlator is required to be greater than 0.9 [20,48]. In order to estimate the demand of the isolation between two input signals for the correlator quickly, we can specify that the variation range of the correlator circle radius is less than 2%. In Figure 4b, it can be seen that the requirement of the isolation between two input signals is larger than 17 dB.

2.3. Influence of Phase Shift Range Error on Correlation Results

As represented in Figure 1, the phase control module is designed in the LO link. Therefore, the phase of the broadband IF signal can be changed by controlling the phase of the LO signal with a single frequency, and the requirements of this system for phase shift are relatively simple. In order to reduce the burden of LO link, a method of directly controlling the phase of RF signals is proposed in this paper, and the proposed phase control module needs to deal with the wideband noise signal. The designed phase shifter needs to ensure that the phase shift range (PSR) of each frequency point is the same under the same control conditions. However, this requirement is difficult to achieve, so this section analyzes the impact of phase shift range error (PSRE) on correlation results.

In the case of broadband range, PSR varies at different frequencies under the same control conditions, and it can be expressed as $\Phi(f)$, which is a function of frequency. Therefore, we can define the phase shift range error (PSRE) as:

$$\Delta\Phi = \Phi_{max}(f_1) - \Phi_{min}(f_2) \quad (9)$$

where $\Delta\Phi$ is the PSR of the phase shifter, Φ_{max} and Φ_{min} are the maximum and minimum phase shift range within the operating frequency band, respectively. It is worth noting that the phase of the RF signal needs to be shifted by 360° to get a complete correlation circle. Since there are two phase shifters on two input channels of the designed chip, the PSR of the designed phase shifter only needs to be greater than 180° .

In order to evaluate the influence of PSRE on the correlation results, it is necessary to analyze the broadband noise characteristics of the analog complex correlator based on six-port technology. The two wideband white noise signals input to the complex correlator can be equivalent to the superposition of multipoint frequency signals. Since the power spectral density of white noise is constant, for the convenience of analysis, we set the amplitude of all frequency points to 1 and the initial phase of two signals θ_1^i and θ_2^i both satisfy the uniform distribution of $0 \sim 2\pi$. Then the two inputs signals can be expressed as

$$\begin{aligned} \tilde{S}_1(t) &= \sum_i \cos(\omega_i t + \theta_1^i) \\ \tilde{S}_2(t) &= \sum_i \cos(\omega_i t + \theta_2^i) \end{aligned} \quad (10)$$

According to Equations (1)–(3), the correlation results for the ideal case can be expressed as:

$$\begin{aligned} V_{real} &= \sum_i G V_{2nd} \cos(\theta_1^i - \theta_2^i) \\ V_{imag} &= \sum_i G V_{2nd} \sin(\theta_1^i - \theta_2^i) \end{aligned} \quad (11)$$

It is assumed that the phase difference of the two broadband noise signals varies with frequency as a constant; that is, the cross-correlation coefficient of the two broadband noise signals is 1. Equation (11) can be simplified as:

$$\begin{aligned} V_{real} &= \sum_i G V_{2nd} \cos(\theta_1 - \theta_2) \\ V_{imag} &= \sum_i G V_{2nd} \sin(\theta_1 - \theta_2) \end{aligned} \quad (12)$$

Due to the PSRE of the phase shifter, a phase shift error (φ^i) will be introduced into the correlation results. Then the correlation results can be expressed as:

$$\begin{aligned} V_{real} &= \sum_i G V_{2nd} \cos(\theta_1 - \theta_2 + \varphi^i) \\ V_{imag} &= \sum_i G V_{2nd} \sin(\theta_1 - \theta_2 + \varphi^i) \end{aligned} \quad (13)$$

The phase shift range of the designed phase shifter changes linearly with the frequency, which will be described in detail in the following section. Then we can assume that the value range of φ^i is $-\Delta\Phi/2 \sim \Delta\Phi/2$ under the condition of taking the center frequency as the reference. Therefore, the variation of the correlation circle and its radius with the PSRE can be obtained in Figure 5. In the same way, the requirement of the PSRE for the correlation system is $\Delta\Phi \leq 19^\circ$.

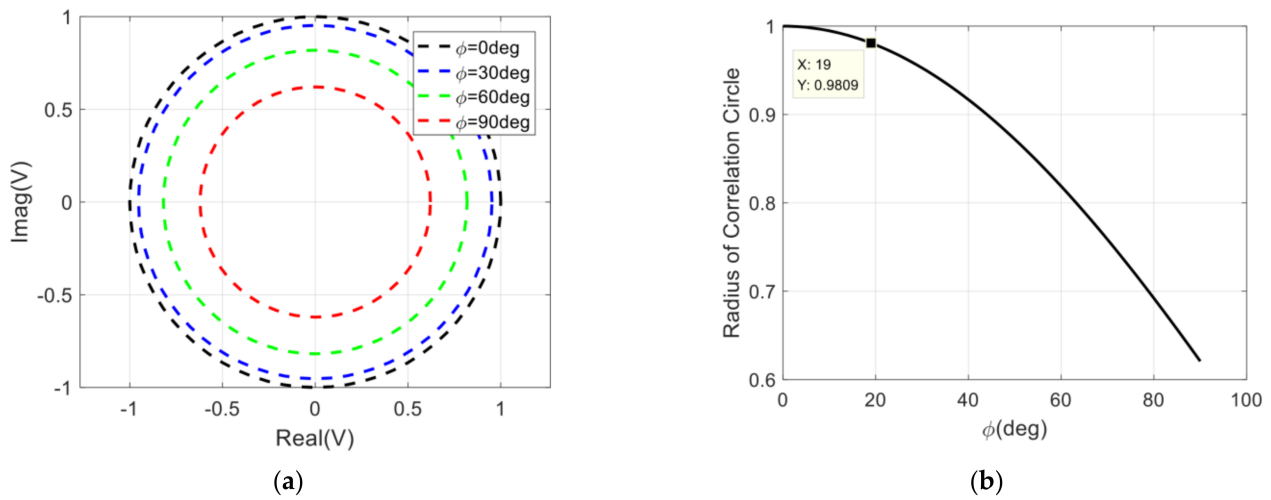


Figure 5. Influence of PSRE on correlation results: (a) The variation of the correlation circle with the PSRE; (b) The variation of the radius of the correlation circle with the PSRE.

2.4. Influence of Isolation in Cross-Over Structure on Correlation Results

As shown in Figure 2, a cross-over structure is used in the six-port network to keep the four outputs on the same side. Therefore it is necessary to evaluate the influence of isolation in the cross-over structure. Assuming that the voltage coupling coefficient in cross-over structure is β , and it varies from 0 to 1. The two inputs are still single-frequency signals $S_1(t)$ and $S_2(t)$, then the four output signals of the six-port network can be described as:

$$\begin{aligned}
 S_3 &= (1 - \beta)S_1 + \sqrt{1 - \beta^2}\hat{S}_2 \\
 S_4 &= (1 + \beta)\hat{S}_1 + \sqrt{1 - \beta^2}S_2 \\
 S_5 &= \sqrt{1 - \beta^2}\hat{S}_1 + \hat{S}_2 + \beta S_2 \\
 S_6 &= -\sqrt{1 - \beta^2}S_1 + S_2 + \beta\hat{S}_2
 \end{aligned} \tag{14}$$

Refer to the derivation process in Section 2.2, after the detector and LPF, the real and imaginary parts of the cross-correlation function can be obtained as:

$$\begin{aligned}
 V_{real} &= GV_{2nd}\sqrt{1 - \beta^2}\cos(\theta_1 - \theta_2) \\
 V_{imag} &= GV_{2nd}\left[\beta + \sqrt{1 - \beta^2}\sin(\theta_1 - \theta_2)\right]
 \end{aligned} \tag{15}$$

Compared to the ideal case, it can be seen that the isolation in the cross-over structure has an influence on the amplitude of the real and imaginary part of the cross-correlation function and adds an additional dc offset error to the imaginary part. Then the variation of the correlation circle and its radius with the isolation in the cross-over structure can be obtained in Figure 6. In the same way, the requirement of the isolation in the cross-over structure for the correlation system is larger than 14 dB.

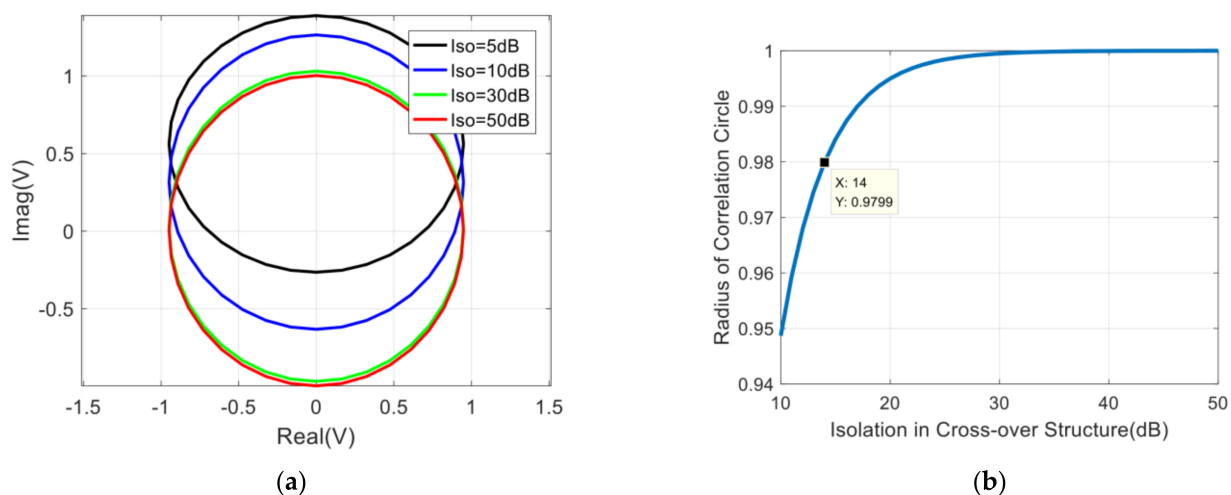


Figure 6. Influence of isolation in cross-over on correlation results: (a) The variation of the correlation circle with the isolation; (b) The variation of the radius of the correlation circle with the isolation.

3. Design of the Integrated Six-Port Chip

As shown in Figure 2, the Ka-band (32–36 GHz) integrated six-port chip, which contains two amplifiers, two phase shifters, and a six-port network is analyzed and designed in this section. In order to reduce the difficulty of design and simulation, we design each single-function circuit first and then simulate the whole circuit. The WIN PL1512 GaAs pHEMT process, which has a nominal cutoff frequency of 95 GHz and features low noise performance, is chosen for the implementation of the circuit. In addition, due to the restriction of processing reticle rules, the size of the chip proposed in this paper is limited to $5\text{ mm} \times 2\text{ mm}$ in order to be processed with other chips together.

3.1. Design of the Amplifier

In terms of the amplifier design, our team has designed and processed a Ka-band amplifier chip based on the same process [49], so the structure of the amplifier in this section is basically the same as the one designed before. Due to the restrictions on the size of the chip, the amplifier is a three-stage amplifier, which is different from the four-stage amplifier processed before. Although the gain of the three-stage amplifier is reduced, when the six-port chip is used as a correlator, an additional amplifier is connected to its four-way output port. The function of the additional amplifier is to amplify the RF signal and provide reverse isolation between the detection circuit and the six-port chip, thereby preventing the influence of the mismatch of the detection circuit on the six-port chip. Therefore, the three-stage amplifier is sufficient for the designed six-port chip. The schematic diagram of the designed amplifier is represented in Figure 7.

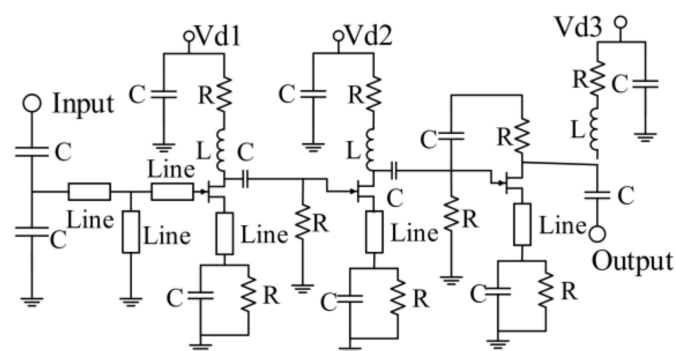


Figure 7. Simplified schematic diagram of the designed three-stage amplifier.

Before the signal enters the chip, it passes through two low-noise amplifiers to meet the noise specification of the system. In addition, the system receives a noise signal; although it has been amplified by the amplifier, the power entering the chip is still low and cannot reach the P_{1dB} of the amplifier. Therefore, the noise figure and P_{1dB} of the designed amplifier is not the key point.

The main function of the amplifier in an integrated six-port chip is to amplify the input signal and compensate for the signal loss caused by the phase shifter and six-port network. The transistors of the designed amplifier with a size of $6 \times 29 \mu\text{m}$, $4 \times 28 \mu\text{m}$, and $2 \times 60 \mu\text{m}$ are used for the first, second, and third stages, respectively. In addition, +3 V DC voltage is used for powering up all the stages, and 2.7 pF by-pass capacitors are also used.

It has been analyzed that the isolation between two amplifiers is important to the analog complex correlator, and the width of the designed chip is only 2 mm. In order to increase isolation between two input amplifiers, the distance between the input ports of the two amplifiers is as far as possible, and an isolation ground is also added in the middle of the two amplifiers. Therefore, the production stage layout design and the simulation results of the proposed two amplifiers are shown in Figure 8.

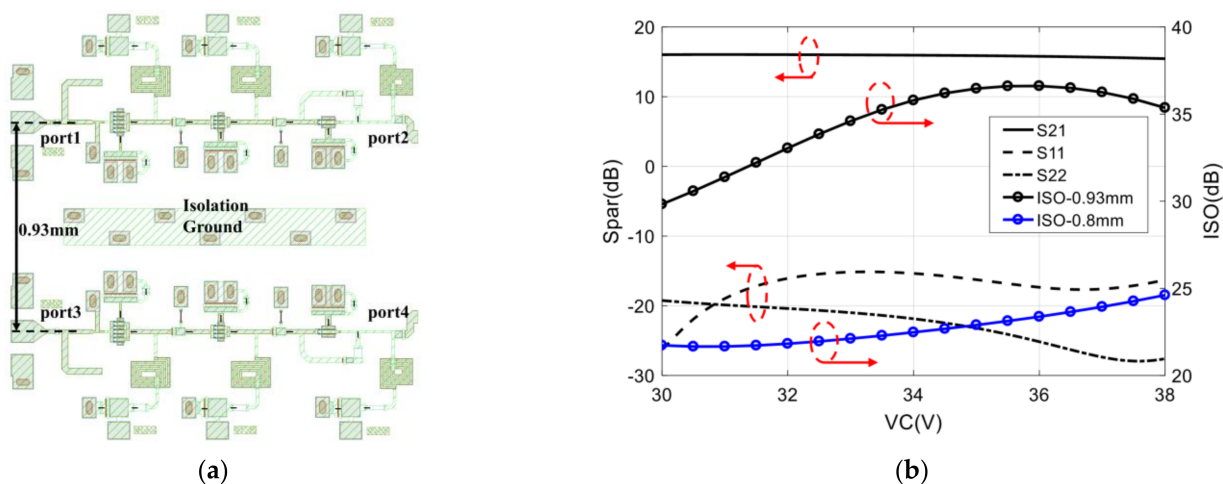


Figure 8. The layout design and the simulation results of the proposed two amplifiers: (a) The production stage layout design; (b) The simulation results.

It can be seen that, from 32–36 GHz, the input return loss (S_{11}) is below -15 dB, the output return loss (S_{22}) is better than -20 dB, the gain (S_{21}) is larger than 15.7 dB, and the in-band gain fluctuation is less than 0.3 dB. In addition, when the distance between two input ports is 0.93 mm, the isolation between two amplifiers, which can be calculated through $dB(S_{21}) - dB(S_{41})$, is larger than 30 dB. When the distance between two input ports is reduced to 0.8 mm, the isolation between the two amplifiers will deteriorate to 21 dB. Therefore, the distance between the two amplifiers should be kept at 0.93 mm to obtain greater isolation.

3.2. Design of the Phase Shifter

As discussed in Section 2.3, the PSR of the designed phase shifter needs to be greater than 180° . Moreover, to get a complete correlation circle, the phase shift of the designed phase shifter is required to be continuously variable; therefore, the analog phase shifter is selected to meet the requirements. In addition, the PSRE requirements of the proposed phase shifter are less than 19° ; this special requirement is relatively rare in general phase shifters [50–55].

The designed phase shifter adopts a combined structure of high-pass phase-shifting and low-pass phase-shifting to minimize PSRE, which is different from the phase shifter that usually only uses a high-pass phase-shifting structure [51]. In order to evaluate the

optimization of the designed phase shifter with high-pass and low-pass structures to PSRE, a phase shifter with a high-pass structure is designed first, which is shown in Figure 9.

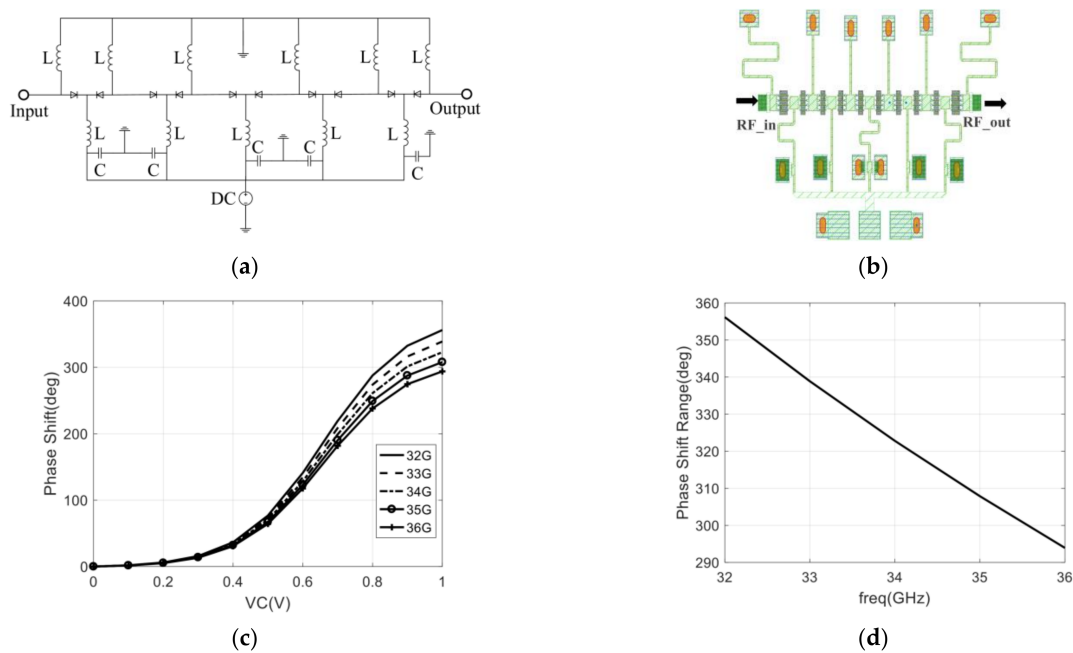


Figure 9. Phase shifter with only high-pass structure: (a) The schematic diagram of designed phase shifter; (b) The layout of designed phase shifter; (c) Simulation result of the phase-shifting with control voltage varying from 0 to 1 V; (d) Phase shift range with the control voltage is 1 V.

It can be seen that the high-pass structure phase shifter utilizes 10 diodes. In the case of control voltage varying from 0 to 1 V, the maximum of the PSR is 356° @ 32 GHz, the minimum of the PSR is 294° @ 36 GHz, and the calculated PSRE is 62° . Moreover, in Figure 9d, we can see that the phase shift range of the designed phase shifter changes linearly with the frequency.

In order to optimize the PSRE, a phase shifter with high-pass and low-pass structures is proposed. As shown in Figure 10, the broadband phase-shifting range of the high-pass and low-pass phase-shifting units are compared, and the results show that the phase-shifting ranges of these two phase-shifting units are complementary in frequency. Therefore, a phase shifter with a high-pass and low-pass structure meets the requirements of the system for PSRE.

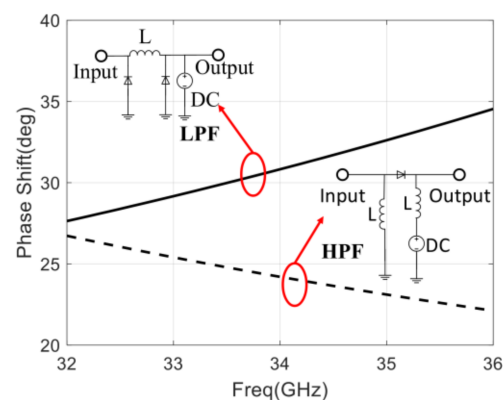


Figure 10. Phase shift range of high-pass and low-pass phase-shifting unit with control voltage varying from 0 to 1 V.

The simplified schematic diagram of the designed phase shifter with high-pass and low-pass structures is shown in Figure 11. From Figure 11a, the diodes of D4–D11 are low-pass phase-shifting structures, and other diodes are high-pass phase-shifting structures. Then, the production stage layout design of the proposed phase shifter is shown in Figure 11b. The size of D2 and D13 diodes are $4 \times 20 \mu\text{m}$, D5 and D10 diodes are $2 \times 35 \mu\text{m}$, D6 and D9 diodes are $2 \times 25 \mu\text{m}$, D7 and D8 diodes are $2 \times 20 \mu\text{m}$, and the rest of the diodes are $4 \times 25 \mu\text{m}$.

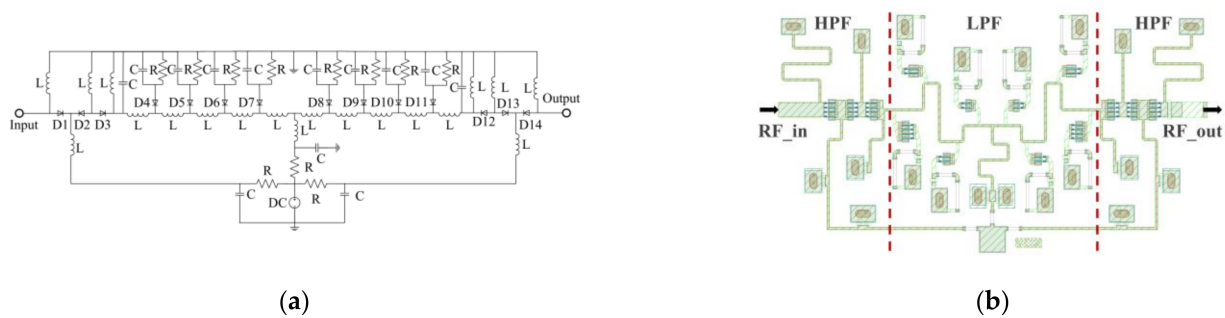


Figure 11. Phase shifter with high-pass and low-pass structure: (a) The schematic diagram of the designed phase shifter; (b) The layout of the designed phase shifter.

The simulation result of the designed phase shifter is shown in Figure 12, and the operating frequency range of the phase shifter is 32–36 GHz. It is worth noting that the state of the phase shifter will change under different control voltages, so there will be different S-parameter simulation results under different control voltages. As shown in Figure 12a, with the control voltage varying from 0 to 1 V, the input and output return loss (S_{11} and S_{22}) is better than -10 dB, and the insertion loss (S_{21}) varies from -5.5 to -7.5 dB. In addition, it can be seen that the maximum of the PSR is 283° @ 32GHz, the minimum of the PSR is 273° @ 36 GHz, which meets the 180° phase shift requirement, and the calculated PSRE is 10° , which is only $1/6$ of the phase shifter with only low-pass structure.

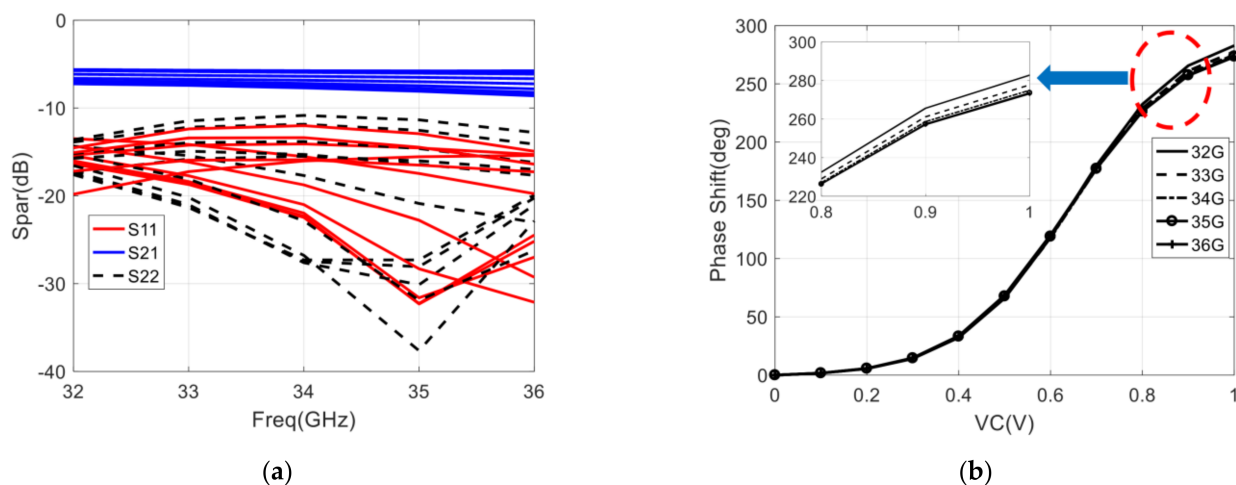


Figure 12. Simulation of the phase shifter: (a) The return loss and the insertion loss with the control voltage varying from 0 to 1 V; (b) Phase shift range.

3.3. Design of the Six-Port Network

The six-port network is a passive microwave system composed of couplers and power dividers. As shown in Figure 2, a cross-over structure is used in the six-port network to keep the four outputs on the same side. In order to increase the isolation of the cross-over structure, a CPWG transmission line is used instead of a microstrip line (MSL), which is represented in Figure 13.

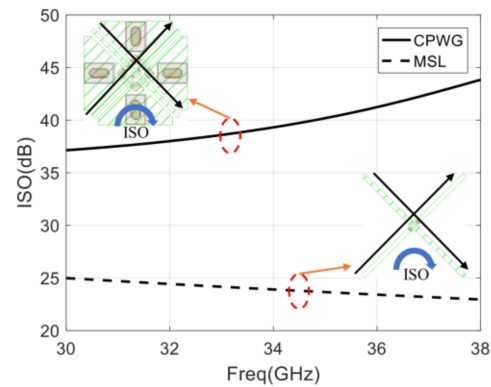


Figure 13. Isolation of the cross-over structure with CPWG and microstrip line.

It can be seen that the isolation of the CPWG transmission line is larger than 38 dB from 32–36 GHz and meets the requirements of the system. Compared with the microstrip transmission line, the isolation is improved by 13 dB.

In this section, the designed six-port network consists of a Wilkinson power divider and three Lange couplers. Therefore, the layout and simulation of the designed six-port is represented in Figure 14.

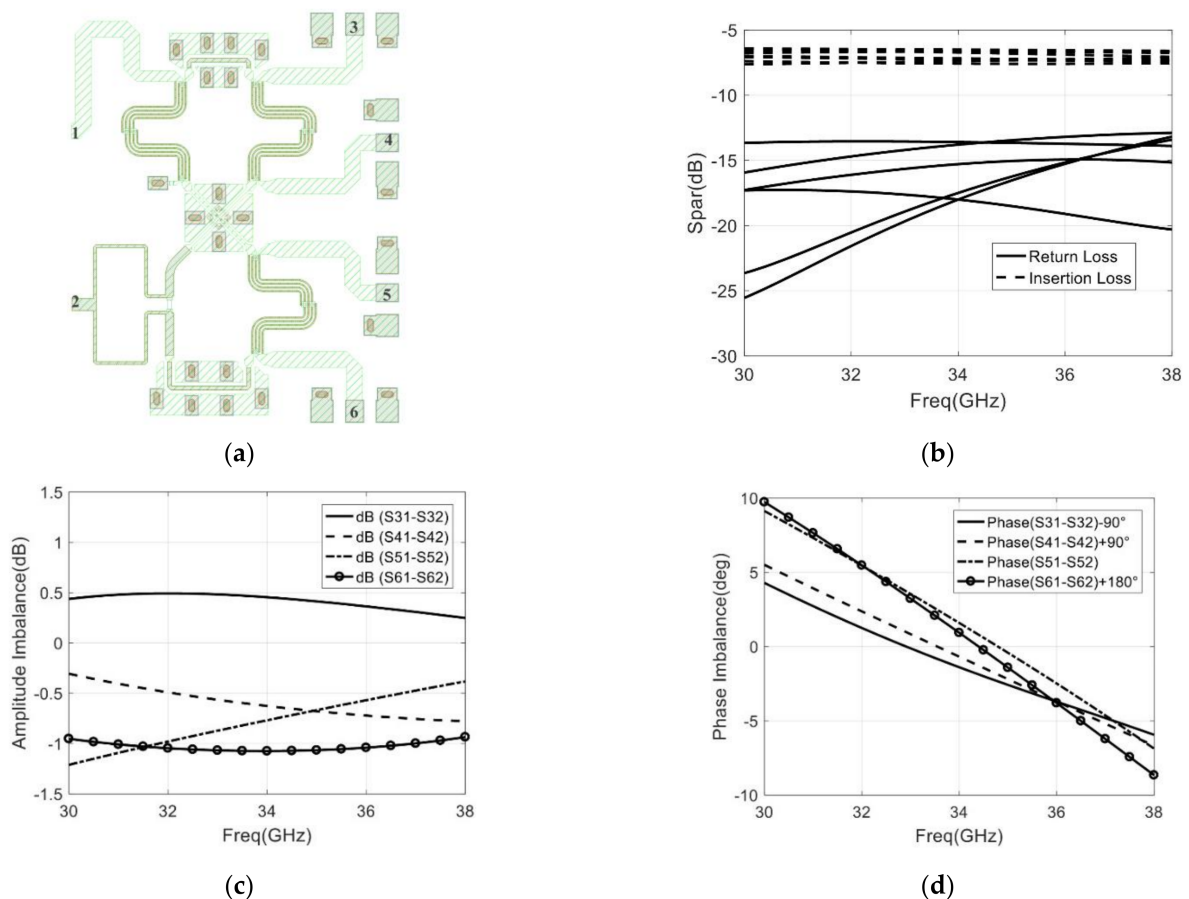


Figure 14. The designed six-port network: (a) Layout design; (b) Simulation of return loss and insertion loss; (c) Simulation of the amplitude imbalance; (d) Simulation of the phase imbalance.

In the operating frequency of 32–36 GHz, the return loss of each port (S_{11} to S_{66}) is below -13 dB, and the insertion loss ($(S_{31} \& S_{32})$ to $(S_{61} \& S_{62})$) varies from -6.5 to -7.5 dB, which is shown in Figure 14b. From Figure 14c,d, the amplitude imbalance is less than ± 1 dB, and the phase imbalance is less than $\pm 5.3^\circ$.

3.4. Simulation of the Integrated Six-Port Chip

According to Figure 2, the layout of the integrated six-port chip can be obtained by combining the three circuits (Amplifier, Phase Shifter, and Six-Port) that have been designed above. The layout of the designed integrated six-port chip is shown in Figure 15, with a chip size of 5 mm × 2 mm.

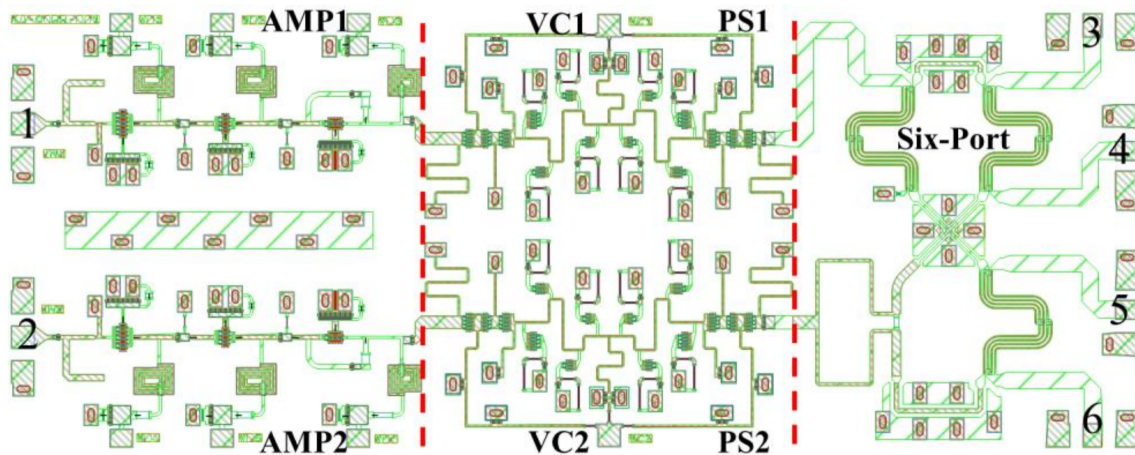


Figure 15. The layout design of the integrated six-port chip with a size of 5 mm × 2 mm. Numbers 1 to 6 represent the port number of the chip.

In order to obtain a complete correlation circle, it is necessary to change the voltage (VC1 and VC2, shown in Figure 15) of the phase shifter. As a result, the performance of the designed six-port chip under different control voltages should be given special attention. Therefore, the simulation result of the designed integrated six-port chip is shown in Figure 16.

In the 32–36 GHz frequency range, the return loss of input ports (S_{11} and S_{22}) with the control voltage varying from 0 to 1 V is below -15 dB, as shown in Figure 16a. It should be noted that the return loss of port 1 varies with the control voltage VC1 and remains unchanged with the change of VC2. Therefore, only the return loss of port 1 with the change in VC1 is given in Figure 16a, and the return loss of port 2 is treated the same way. Furthermore, the return loss of output ports (S_{33}) to (S_{66}) with the control voltage varying from 0 to 1 V is below -13 dB. In Figure 16b, we can see that the gain of the four output ports varies from -2 to 5 dB with the control voltage varying from 0 to 1 V. The PSR of two-phase shifters, shown in Figure 16c,d, respectively, is larger than 265° with the control voltage varying from 0 to 1 V, and the calculated PSRE is 9° . In addition, the amplitude and phase imbalance of four output ports also varies with the control voltage (both VC1 and VC2) varying from 0 to 1 V. Due to the huge amount of data on this technical indicator, this article only gives a statistical result. The amplitude imbalance is less than ± 5 dB, and the imbalance is less than $\pm 15^\circ$ with the control voltage (both VC1 and VC2) varying from 0 to 1 V.

Assuming the detector and differential amplifier behind the designed chip are ideal, we can obtain the correlation circle by changing the control voltage of the phase shifter. The simulation of the correlation circle is represented in Figure 17.

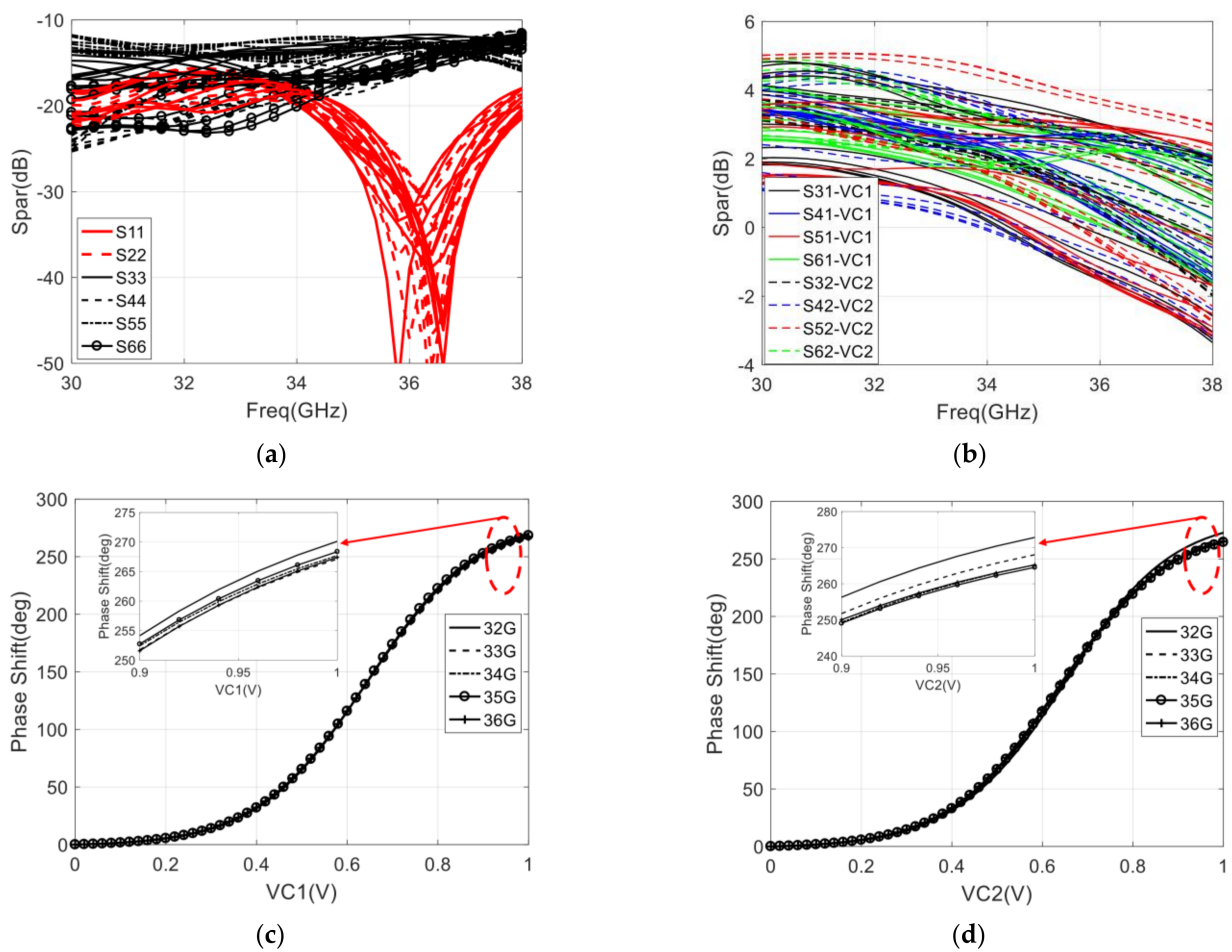


Figure 16. Simulation result of the integrated six-port chip with control voltage varying from 0 to 1 V: (a) Return loss of each port; (b) The gain of four output ports; (c) Phase shift range with control voltage (VC1) variances; (d) Phase shift range with control voltage (VC2) variances.

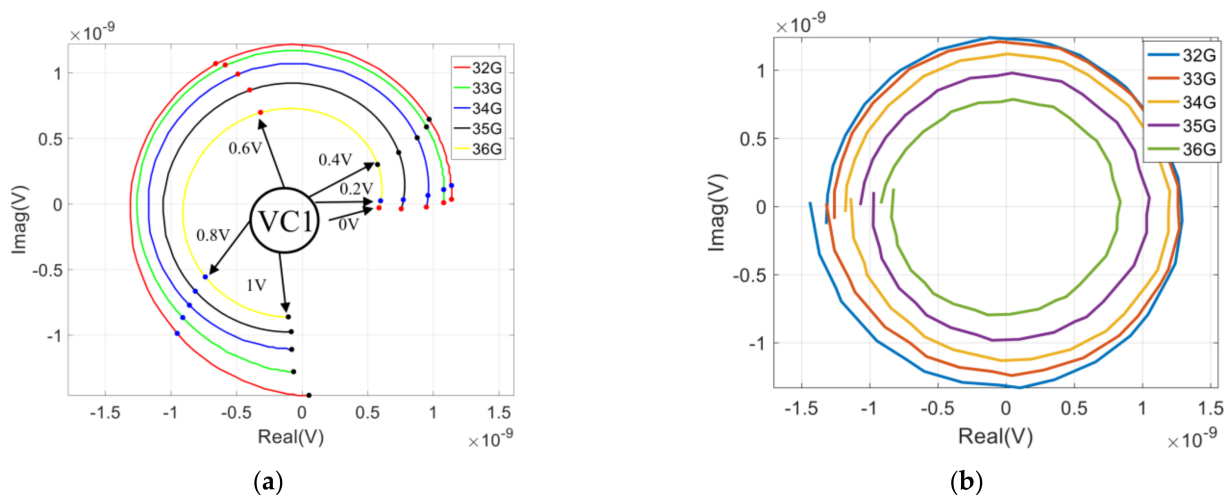


Figure 17. The simulation of the correlation circle: (a) The control voltage of only one phase shifter (VC1) varies; (b) The control voltage of both phase shifters varies.

As represented in Figure 17a, the correlation circle is not closed by using only one control voltage (VC1) of the phase shifter, and the phase difference between two input signals varies from 0° to 265°. Moreover, a complete correlation circle can be formed by

selecting both control voltages (VC1 and VC2), which is shown in Figure 17b, and the phase difference between the two input signals vary from -180° to 180° .

4. Measurement of the Integrated Six-Port Chip

The microphotograph of the fabricated integrated six-port chip is shown in Figure 18a, with a chip size of $5\text{ mm} \times 2\text{ mm}$, and a printed-circuit-board test fixture, which is designed using a 5-mil thickness Rogers 3003 substrate with $50\ \Omega$ microstrip, is taken for the measurement of the integrated six-port chip. Bond-wires are constructed for the interconnections of the chip and the input–output microstrip transmission lines. High-frequency K connectors and matching loads are employed for the measurements. As required by the chip, the DC voltage of the amplifier is 3 V, and the total consumed current is 73 mA.

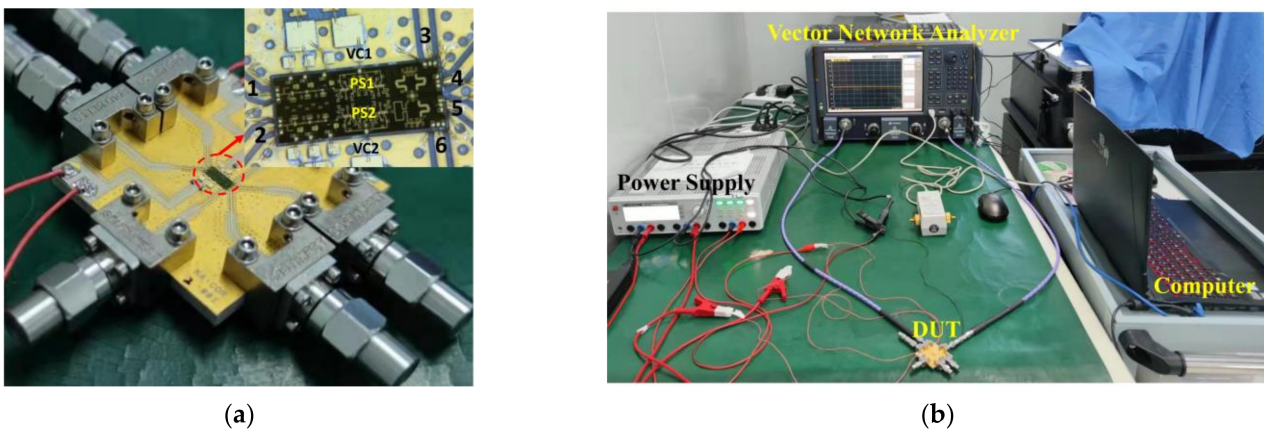


Figure 18. The photograph of the fabricated chip and test platform: (a) The microphotograph of the fabricated integrated six-port chip and test fixture; (b) The photograph of the automatic test platform for the integrated six-port chip.

The Keysight N5227B vector network analyzer and Rohde & Schwarz HMP 2030 programmable power supply are used for the measurement, shown in Figure 18b.

4.1. Measurement of the Return Loss, Gain, and Phase Shift Range

The measurement result of return loss, gain, and phase shift range is represented in Figure 19. To measure the phase-shifting curve of the integrated six-port chip, we can observe the phase of the output port signal by changing the control voltage of the phase shifter. Because the six-port chip has four output ports, four phase-shifting curves can be measured, and the final phase-shifting curve can be obtained by averaging these four curves.

The final phase-shifting curve of PS1 (which is described in Figure 18a) is shown in Figure 19d. It can be seen that the PSR is larger than 200° with the control voltage varying from 0 to 1 V, and the PSR can still be increased to 222° by the control voltage varying from 1 to 1.5 V, and the PSR of phase shifter meets the 180° phase shift requirement. Therefore, the calculated PSRE is 8.2° and 9.5° with the control voltage varying from 0 to 1 V and 0 to 1.5 V, respectively. The phase shift range of the phase shifter is still increasing when the control voltage is greater than 1 V and is basically unchanged when the control voltage is greater than 1.5 V. It is recommended that the control voltage range of the phase shifter is 0 to 1.5 V during practical application. The range of control voltage is also used in the measurement of return loss and gain.

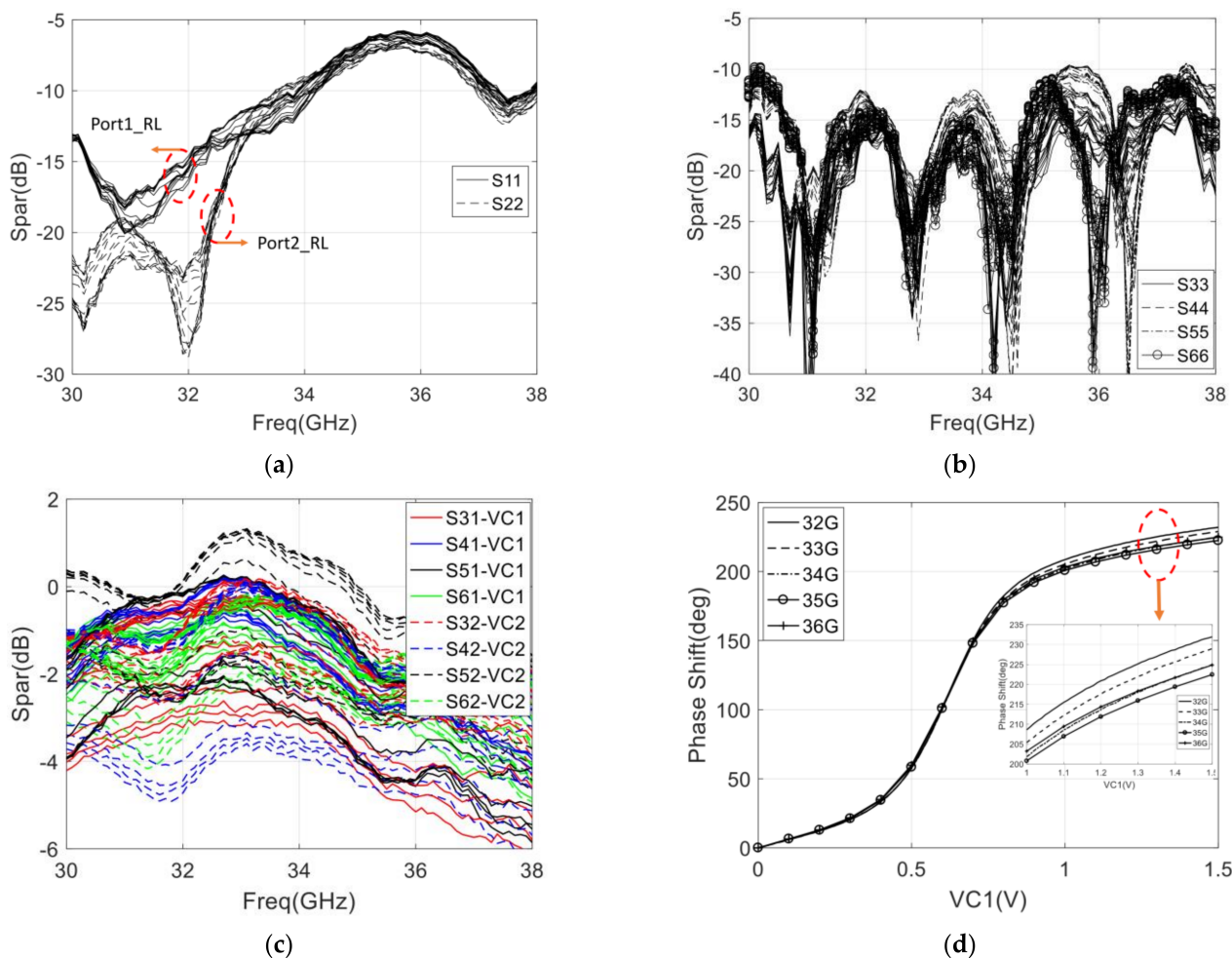


Figure 19. Simulation result of the integrated six-port chip with control voltage varying from 0 to 1 V: (a) Return loss of each port; (b) The gain of four output ports; (c) Phase shift range with control voltage (VC1) variances; (d) Phase shift range with control voltage (VC2) variances.

Since the state of the designed chip is different under different control voltages, it is necessary to measure the S-parameters under each control voltage to evaluate the overall performance of the designed chip, and Figure 19a–c show the measured return loss and insertion loss under different control voltages. As shown in Figure 19a, the return loss of input ports with control voltage varying from 0 to 1.5 V is below -10 dB with the frequency range of 32–34 GHz, and the return loss is below -5.9 dB with the frequency range of 32–36 GHz. It can be seen that the return loss of the input port is deteriorated due to the frequency offset. Moreover, the return loss of output ports with control voltage varying from 0 to 1.5 V is below -10 dB, which is shown in Figure 19b. The return loss of four output ports is basically consistent with the simulation results. In Figure 19c, we can see that the gain of four output ports varies from -5 to 1 dB with the control voltage varying from 0 to 1.5 V. From the statistics of the measurement, the gain is about 4 dB lower than that of the simulation.

Compared with the simulation result, the measured return loss of the designed chip has deteriorated, especially in frequencies above 34 GHz. The reason for the return loss deterioration and gain reduction is that there is a deviation between the simulation model and actual parameters in the Ka-band when the chip is fabricated using $0.15\text{-}\mu\text{m}$ GaAs pHEMT technology.

In addition, the statistical result of the amplitude imbalance is less than ± 4 dB, and the phase imbalance is less than $\pm 20^\circ$ with the control voltage (both VC1 and VC2) varying from 0 to 1.5 V, which is not shown in the figure of this section.

4.2. Measurement of the Isolation between Two Amplifiers

In order to measure the isolation between two amplifiers of the six-port chip, the influence of isolation between two amplifiers on four output ports of the six-port chip is analyzed first. Assuming that the inputs are two single-frequency signals $S_1(t)$ and $S_2(t)$, the voltage coupling coefficient between the two amplifiers is α , and the phase shift angles of PS1 and PS2 are φ_1 and φ_2 , respectively. Therefore the two input signals of the six ports can be expressed as:

$$\begin{aligned} S'_1 &= \sqrt{1-\alpha^2}e^{j\varphi_1}S_1 + \alpha e^{j\varphi_1}S_2 \\ S'_2 &= \alpha e^{j\varphi_2}S_1 + \sqrt{1-\alpha^2}e^{j\varphi_2}S_2 \end{aligned} \quad (16)$$

If only the control voltage (VC2) of the PS2 is changed, and the signal is only provided at port 1, the value of φ_2 and $S_2(t)$ is 0. Then, the signals of the four output ports can be expressed as:

$$\begin{aligned} S_{31} &= \sqrt{1-\alpha^2}S_1 + \alpha e^{j(\varphi_2+90^\circ)}S_1 \\ S_{41} &= \sqrt{1-\alpha^2}e^{j(90^\circ)}S_1 + \alpha e^{j(\varphi_2)}S_1 \\ S_{51} &= \sqrt{1-\alpha^2}e^{j(90^\circ)}S_1 + \alpha e^{j(\varphi_2+90^\circ)}S_1 \\ S_{61} &= -\sqrt{1-\alpha^2}S_1 + \alpha e^{j(\varphi_2)}S_1 \end{aligned} \quad (17)$$

Similarly, if only the control voltage (VC1) of the PS1 is changed, and the signal is only provided at port 2, the value of φ_2 and $S_1(t)$ is 0, and the signals of the four output ports can be expressed as:

$$\begin{aligned} S_{32} &= \sqrt{1-\alpha^2}e^{j(90^\circ)}S_2 + \alpha e^{j(\varphi_1)}S_2 \\ S_{41} &= \sqrt{1-\alpha^2}S_2 + \alpha e^{j(\varphi_1+90^\circ)}S_2 \\ S_{51} &= \sqrt{1-\alpha^2}e^{j(90^\circ)}S_2 + \alpha e^{j(\varphi_1+90^\circ)}S_2 \\ S_{61} &= \sqrt{1-\alpha^2}S_2 + \alpha e^{j(\varphi_1)}S_2 \end{aligned} \quad (18)$$

It is noteworthy that the above derivation only considers the amplitude coefficient of the coupled signal and does not include the phase of the coupled signal. However, the isolation between the two amplifiers can still be estimated by calculating the maximum amplitude or phase error of the output port signal by changing the phase of the phase shifter, which can be expressed as:

$$\begin{aligned} A_{max} &= 20 \log \left(\frac{\sqrt{1-\alpha^2}+\alpha}{\sqrt{1-\alpha^2}-\alpha} \right) \\ \Psi_{max} &= 2 * \arctan \left(\frac{\alpha}{\sqrt{1-\alpha^2}} \right) \end{aligned} \quad (19)$$

where A_{max} and Ψ_{max} are the maximum amplitude error and phase error, respectively. As the value range of α is 0 to 1, we can replace α with $\sin \delta$, and the value range of δ is 0 to $\pi/2$, then Equation (19) can be simplified as:

$$\begin{aligned} A_{max} &= 20 \log \left(\frac{\cos \delta + \sin \delta}{\cos \delta - \sin \delta} \right) \\ \Psi_{max} &= 2 * \arctan (\tan \delta) \end{aligned} \quad (20)$$

From Equations (8), (19) and (20), the isolation between two amplifiers can be expressed as:

$$\begin{aligned} ISO &= -20 \log \left(\sin \left(\arctan \left(10^{\frac{A_{max}}{20}} \right) - 45^\circ \right) \right) \\ &= -20 \log \left(\sin \left(\frac{\Psi_{max}}{2} \right) \right) \end{aligned} \quad (21)$$

In the measurement stage, the control voltage (VC2) of the PS2 is changed, as shown in Figure 18a, when the signal is provided at port 1 and not provided at port 2, and the isolation between the two amplifiers can be determined by measuring the change of the amplitude and phase of the signal at the output port. The isolation can be determined by changing VC1 and providing a signal to port 2 as well. The measurement of the amplitude and phase fluctuation with the change in the control voltage (VC1 or VC2) is shown in Figure 20.

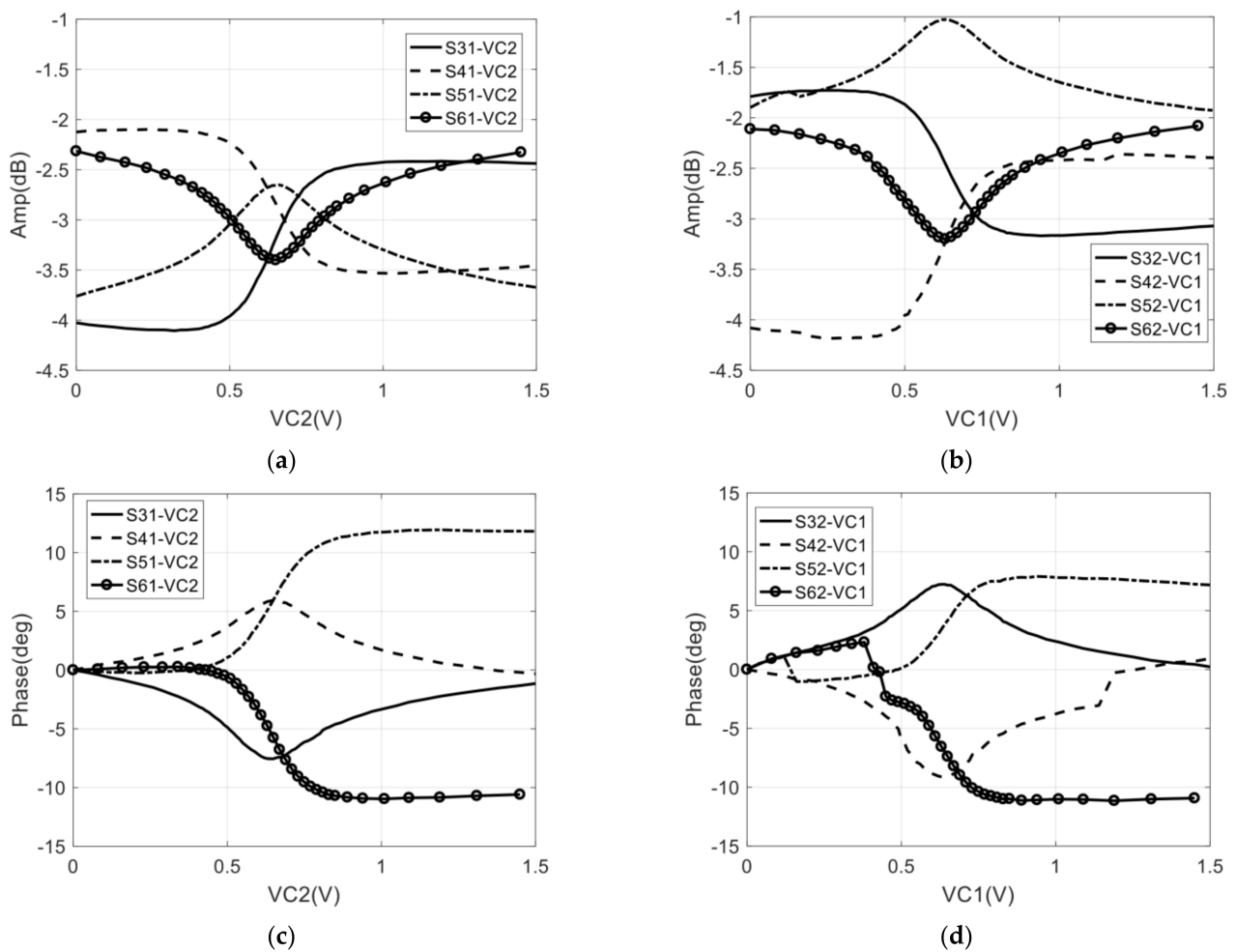


Figure 20. Measurement of the amplitude and phase fluctuation with the change in the control voltage @ 34 GHz: (a) Amplitude fluctuation with change of VC2 and input of port 1; (b) Amplitude fluctuation with change of VC1 and input of port 2; (c) Phase fluctuation with change of VC2 and input of port 1; (d) Phase fluctuation with change of VC1 and input of port 2.

As shown in Figure 20, in the case of change of VC2 and input of port 1 or change of VC1 and input of port 2, the amplitude and phase of the output signals of the four ports will change with the control voltage. It means that the isolation between the two amplifiers can be calculated through the maximum amplitude/phase error of four output signals.

In the 32–36 GHz frequency range, the maximum amplitude/phase error of four output ports and the calculated isolation are shown in Figure 21. As shown in Figure 21c, the calculated average isolation is larger than 20 dB, and the isolation calculated by A_{max} and Ψ_{max} has good consistency.

Then, the comparison between simulation and measurement of the designed integrated six-port chip is shown in Table 1. It can be seen that, compared with the simulation results, the measurement results of various indicators have a certain degree of deterioration, but the most important indicators of PSR, PSRE, and the isolation between two amplifiers meet the requirements of the system.

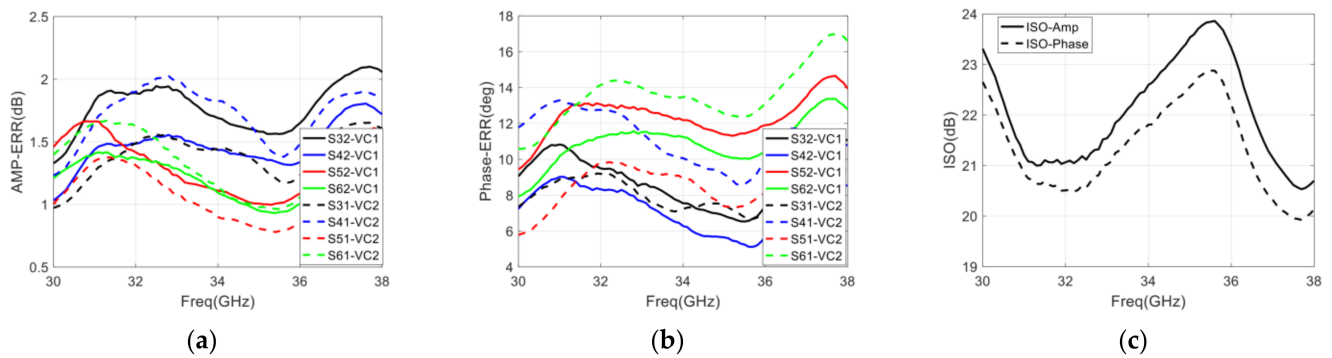


Figure 21. The maximum amplitude/phase error and calculated isolation between two amplifiers: (a) Maximum amplitude error of four output ports; (b) Maximum phase error of four output ports; (c) The calculated average isolation through maximum amplitude and phase error, respectively.

Table 1. The comparison between simulation and measurement of the designed six-port chip.

Parameter	Simulation	Measurement
Control voltage (V)	0–1	0–1.5
Phase shift range (deg)	≥ 265	≥ 222
Phase shift range error (deg)	≤ 10	≤ 10
Isolation between two amplifiers (dB)	≥ 30	≥ 20

Since this chip integrates functions such as phase-shifting and six-port circuits, it is compared with others' work in terms of phase-shifting and six-port circuits, which is shown in Tables 2 and 3.

Table 2. Comparison table of the six-port circuit.

Reference	This Work	[29]	[32]
Process	0.15- μm GaAs	Waveguide	130 nm COMS
Freq (GHz)	32–36	15–20	60–65
Amplitude Imbalance (dB)	$-2 \pm 2.5^*$	-6 ± 2.2	-6 ± 1
Phase Imbalance (deg)	$\pm 5^*$	± 15	± 5
Return Loss (dB)	$< -11^\#$	< -12	< -12

* The control voltage of the six-port chip (VC1 and VC1) is 0 V. # The return loss of four output ports.

Table 3. Comparison table of phase shifters.

Reference	This Work	[52]	[54]	[55]
Process	0.15- μm GaAs	180-nm COMS	90-nm COMS	130-nm COMS
Freq (GHz)	32–36	15–20	57–64	21–24
PSR (deg)	≥ 222	360	360	≥ 290
PSRE (deg)	≤ 10	–	–	–
Gain (dB)	-2 ± 3	-5 ± 5	-8.5 ± 4.5	-7.4 ± 4.5

5. Conclusions

In order to carry on the correlation processing directly to the RF signal and reduce the burden of LO link on the interferometric passive millimeter-wave imaging system, a Ka-band (32–36 GHz) six-port chip integrated with two amplifiers, two phase shifters, and a six-port network is designed and fabricated based on 0.15- μm GaAs pHEMT technology. At the design stage, the influence of the isolation between two amplifiers, PSRE, and isolation in the cross-over structure on the correlation results are analyzed and simulated.

Then a wideband phase shifter with a low-pass and high-pass structure is designed, and the simulated PSR and PSRE of the phase shifter are 265° and 10° , respectively, with the control voltage varying from 0 to 1 V. Finally, the performance of the designed integrated six-port chip, with a size of $5\text{ mm} \times 2\text{ mm}$, is simulated. At the measurement stage, the return loss and gain of the chip have a certain degree of deterioration compared with the simulation result. With the control voltage varying from 0 to 1.5 V, the PSR and PSRE of the phase shifter are 222° and 10° , respectively, which meets the requirements of the system. The measurement method of isolation between two amplifiers is analyzed and verified, and the final measurement result of isolation is greater than 20 dB, which also meets the requirements of the system.

Author Contributions: Conceptualization, J.M.; methodology, W.H., X.C. and J.G.; validation, W.H., X.C. and J.G.; formal analysis, W.H.; investigation, W.H.; resources, J.M. and A.H.; data curation, W.H.; writing—original draft preparation, W.H.; writing—review and editing, X.C. and J.G.; visualization, W.H.; supervision, J.M.; project administration, A.H.; funding acquisition, J.M. and A.H. All authors have read and agreed to the published version of the manuscript.

Funding: This work was supported in part by the National Nature Science Foundation Program of China under Grant 61731001 and in part by the Shanghai Aerospace Science and Technology Innovation Fund under Grant SAST2020-081.

Institutional Review Board Statement: Not applicable.

Informed Consent Statement: Not applicable.

Data Availability Statement: Not applicable.

Conflicts of Interest: The authors declare no conflict of interest.

References

1. Engen, G.F. The Six-Port Reflectometer: An Alternative Network Analyzer. *IEEE Trans. Microw. Theory Tech.* **1977**, *25*, 1075–1080. [[CrossRef](#)]
2. Engen, G.F. An Overview of the Six-Port Measurement Technique. In Proceedings of the IEEE-MTT-S International Microwave Symposium Digest, Ottawa, ON, Canada, 27–29 June 1978; pp. 174–175.
3. Hoer, C.A. The Six-Port Coupler: A New Approach to Measuring Voltage, Current, Power, Impedance, and Phase. *IEEE Trans. Instrum. Meas.* **1972**, *21*, 466–470. [[CrossRef](#)]
4. Fadhel, G.; Abbas, M. *The Six-Port Technique with Microwave and Wireless Applications*; Artech: London, UK, 2009.
5. Julrat, S.; Trabelsi, S. Portable Six-Port Reflectometer for Determining Moisture Content of Biomass Material. *IEEE Sensors J.* **2017**, *17*, 4814–4819. [[CrossRef](#)]
6. Staszek, K.; Gruszczynski, S.; Wincza, K. Six-Port Reflectometer Providing Enhanced Power Distribution. *IEEE Trans. Microw. Theory Tech.* **2016**, *64*, 939–951. [[CrossRef](#)]
7. Gutierrez Miguelez, C.; Huyart, B.; Bergeault, E.; Jallet, L.P. A new automobile radar based on the six-port phase/frequency discriminator. *IEEE Trans. Veh. Technol.* **2000**, *49*, 1416–1423. [[CrossRef](#)]
8. Tatu, S.O.; Wu, K.; Denidni, T.A. Direction-of-arrival estimation method based on six-port technology. *IEE Proc.-Microwaves, Antennas Propag.* **2006**, *153*, 263–269. [[CrossRef](#)]
9. Vinci, G.; Koelpin, A. Progress of Six-Port technology for industrial radar applications. In Proceedings of the 2016 IEEE Topical Conference on Wireless Sensors and Sensor Networks (WiSNet), Austin, TX, USA, 24–27 January 2016; pp. 48–51.
10. Vinci, G.; Lindner, S.; Barbon, F.; Mann, S.; Hofmann, M.; Duda, A.; Weigel, R.; Koelpin, A. Six-Port Radar Sensor for Remote Respiration Rate and Heartbeat Vital-Sign Monitoring. *IEEE Trans. Microw. Theory Tech.* **2013**, *61*, 2093–2100. [[CrossRef](#)]
11. Joy, E.; Leach, W.; Rodrigue, G. Applications of probe-compensated near-field measurements. *IRE Trans. Antennas Propag.* **1978**, *26*, 379–389. [[CrossRef](#)]
12. Pereira, J.F.R.; Anderson, A.P.; Bennett, J.C. New procedure for near-field measurements of microwave antennas without anechoic environments. *Microw. Opt. Antennas IEE Proc. H.* **1984**, *131*, 351–358. [[CrossRef](#)]
13. Yujiri, L.; Shoucri, M.; Moffa, P. Passive millimeter-wave imaging. *IEEE Micro.* **2003**, *4*, 39–50. [[CrossRef](#)]
14. Ryman, E.; Emrich, A.; Andersson, S.B.; Svensson, L.; LarssonEdefors, P. 1.6 GHz Low-Power Cross-Correlator System Enabling Geostationary Earth Orbit Aperture Synthesis. *IEEE J. Solid-State Circuits* **2014**, *49*, 2720–2729. [[CrossRef](#)]
15. Bell, J.; Knag, P.; Sun, S.; Lim, Y.; Chen, T.; Fredenburg, J.; Chen, C.-H.; Zhai, C.; Rocca, A.; Collins, N.; et al. A 1.5-GHz 6.144T Correlations/s 64×64 Cross-Correlator with 128 Integrated ADCs for Real-Time Synthetic Aperture Imaging. *IEEE J. Solid-state Circuits* **2017**, *52*, 1450–1457. [[CrossRef](#)]

16. Li, C.-T.; Kubo, D.; Han, C.-C.; Chen, C.-C.; Chen, M.-T.; Lien, C.-H.; Wang, H.; Wei, R.-M.; Yang, C.-H.; Chiueh, T.-D.; et al. A wideband analog correlator system for AMiBA. *Proc. SPIE*. **2004**, *5498*, 455–464. [[CrossRef](#)]
17. Padin, S. A wideband analog continuum correlator for radio astronomy. *IEEE Trans. Instrum. Meas.* **1994**, *43*, 782–785. [[CrossRef](#)]
18. Li, C.-T.; Kubo, D.Y.; Wilson, W.; Lin, K.-Y.; Chen, M.-T.; Ho, P.; Chen, C.-C.; Han, C.-C.; Oshiro, P.; Martin-Cocher, P.; et al. AMIBA wideband analog correlator. *Astrophys. J. Lett.* **2010**, *716*, 746–757. [[CrossRef](#)]
19. Shenoy, V.; Jung, S.; Yoon, Y.; Park, Y.; Kim, H.; Chung, H.-J. A CMOS Analog Correlator-Based Painless Nonenzymatic Glucose Sensor Readout Circuit. *IEEE Sens. J.* **2014**, *14*, 1591–1599. [[CrossRef](#)]
20. Koistinen, O.; Lahtinen, J.; Hallikainen, M.T. Comparison of analog continuum correlators for remote sensing and radio astronomy. *IEEE Trans. Instrum. Meas.* **2002**, *51*, 227–234. [[CrossRef](#)]
21. Javed, A.R.; Scheytt, J.C.; Ahe, U.V.D. Linear ultra-broadband NPN-only analog correlator at 33 Gbps in 130 nm SiGe BiCMOS technology. In Proceedings of the IEEE Bipolar/BiCMOS Circuits and Technology Meeting (BCTM), New Brunswick, NJ, USA, 25–27 September 2016; pp. 78–81.
22. Wang, C.; Xin, X.; Kashif, M.; Miao, J. A Compact Analog Complex Cross-Correlator for Passive Millimeter-Wave Imager. *IEEE Trans. Instrum. Meas.* **2017**, *66*, 2997–3006. [[CrossRef](#)]
23. Seong, J.-T.; Kim, S.-H.; Kim, Y.-H. Error analysis of an analog correlator for polarimetry. *IEICE Electron. Express* **2018**, *15*, 20171207. [[CrossRef](#)]
24. Gilbert, B. A precise four-quadrant multiplier with subnanosecond response. *IEEE J. Solid-State Circuits* **1968**, *3*, 365–373. [[CrossRef](#)]
25. Kashif, M.; Hu, A.; Miao, J. Design and Implementation of an Analog Complex Correlator for Passive Millimeter Wave Imaging System. In Proceedings of the 13th International Bhurban Conference on Applied Sciences and Technology (IBCAST), Islamabad, Pakistan, 12–16 January 2016; pp. 611–616.
26. Holler, C.M.; Kaneko, T.; Jones, M.E.; Grainge, K.; Scott, P. A 6–12 GHz analogue lag-correlator for radio interferometry. *Astron. Astrophys.* **2007**, *464*, 795–806. [[CrossRef](#)]
27. Ryle, M. A New Radio Interferometer and Its Application to the Observation of Weak Radio Stars. *Proc. R. Soc. London A Math. Phys. Eng. Sci.* **1952**, *211*, 351–375. [[CrossRef](#)]
28. Chen, C.; Mehdi, G.; Wang, C.; Dilshad, U.; Hu, A.; Miao, J. A GaAs Power Detector Design for \$C\\$\$-Band Wideband Complex Cross Correlation Measurement. *IEEE Trans. Instrum. Meas.* **2020**, *69*, 5673–5683. [[CrossRef](#)]
29. Sakr, A.A.; Dyab, W.M.; Wu, K. A Dually Polarized Six-Port Junction Based on Polarization-Selective Coupling for Polarization-Inclusive Remote Sensing. *IEEE Trans. Microw. Theory Tech.* **2018**, *66*, 3817–3827. [[CrossRef](#)]
30. Ardakani, M.D.; Tatu, S.O. V-Band Six-Port Interferometer Receiver: High Data-Rate Wireless Applications, BER and EVM Analysis, and CFO Compensation. *IEEE Access* **2021**, *9*, 160847–160854. [[CrossRef](#)]
31. Moghaddasi, J.; Wu, K. Multifunction, Multiband, and Multimode Wireless Receivers: A Path toward the Future. *IEEE Microw. Mag.* **2020**, *21*, 104–125. [[CrossRef](#)]
32. Hannachi, C.; Tatu, S.O. A new compact V-band six-port receiver for high data-rate wireless applications. In Proceedings of the IEEE Topical Conference on Wireless Sensors and Sensor Networks (WiSNet), San Diego, CA, USA, 25–28 January 2015; pp. 26–28.
33. Zhang, H.; Li, L.; Wu, K. Software-Defined Six-Port Radar Technique for Precision Range Measurements. *IEEE Sensors J.* **2008**, *8*, 1745–1751. [[CrossRef](#)]
34. Vinci, G.; Barbon, F.; Lindner, S.; Weigel, R.; Koelpin, A. Six-port based high-resolution smart antenna alignment sensor. In Proceedings of the IEEE-APS Topical Conference on Antennas and Propagation in Wireless Communications (APWC), Cape Town, South Africa, 2–7 September 2012; pp. 280–283.
35. Arshad, N.S.A.; Ibrahim, S.Z.; Razalli, M.S. Six-port demodulator in homodyne direct conversion receiver. In Proceedings of the 2nd International Conference on Electronic Design (ICED), Penang, Malaysia, 19–21 August 2014; pp. 499–504.
36. Talebzadeh, A.; Abdipour, A. Miniaturized six-port receiver for 60 GHz communication. In Proceedings of the 22nd Iranian Conference on Electrical Engineering (ICEE), Tehran, Iran, 20–22 May 2014; pp. 1406–1410.
37. Lan, M.; Wu, Y.; Huang, Z.; Liu, H.; Zhao, C.; Yu, Y.; Kang, K. An Improved Six-Port Equivalent-Circuit Model for Millimeter-Wave On-Chip Transformers with Accurate Coupling Factor Modeling. *IEEE Trans. Microw. Theory Tech.* **2021**, *69*, 3989–4000. [[CrossRef](#)]
38. Wang, C.-H.; Chang, H.-Y.; Wu, P.S.; Lin, K.-Y.; Huang, T.-W.; Wang, H.; Chen, C.H. A 60 GHz Low-Power Six-Port Transceiver for Gigabit Software-Defined Transceiver Applications. In Proceedings of the IEEE International Solid-State Circuits Conference. Digest of Technical Papers, San Francisco, CA, USA, 11–15 February 2007; pp. 192–596.
39. Laemmle, B.; Schmalz, K.; Borngraeber, J.; Scheytt, J.C.; Weigel, R.; Koelpin, A.; Kissinger, D. A fully integrated 120-GHz six-port receiver frontend in a 130-nm SiGe BiCMOS technology. In Proceedings of the IEEE 13th Topical Meeting on Silicon Monolithic Integrated Circuits in RF Systems, Austin, TX, USA, 21–23 January 2013; pp. 129–131.
40. Voelkel, M.; Hirsch, H.; Dietz, M.; Weigel, R.; Hagelauer, A.; Kissinger, D. A Low-Power 120-GHz integrated six-port receiver front-end with digital adjustable gain in a 130-nm bicos technology. In Proceedings of the IEEE Bipolar/BiCMOS Circuits and Technology Meeting (BCTM), Nuremberg, Germany, 8–10 October 2017; pp. 82–85.
41. Vakalis, S.; Nanzer, J.A. Towards Three-Dimensional Active Incoherent Millimeter-Wave Imaging. In Proceedings of the IEEE International Conference on Autonomous Systems (ICAS), Montreal, QC, Canada, 11–13 August 2021; pp. 1–5.

42. Vakalis, S.; Gong, L.; He, Y.; Papapolymerou, J.; Nanzer, J.A. Experimental Demonstration and Calibration of a 16-Element Active Incoherent Millimeter-Wave Imaging Array. *IEEE Trans. Microw. Theory Tech.* **2020**, *68*, 3804–3813. [[CrossRef](#)]
43. Skou, N. *Microwave Radiometer Systems: Design and Analysis*; Artech House: Norwood, MA, USA, 1989.
44. Guo, X.; Asif, M.; Hu, A.; Li, Z.; Miao, J. A 1-GHz 64-Channel Cross-Correlation System for Real-Time Interferometric Aperture Synthesis Imaging. *Sensors* **2019**, *19*, 1739. [[CrossRef](#)]
45. Wang, C.; Ye, X.; Chen, X.; Xin, X.; Liang, B.; Li, Z.; Hu, A.; Miao, J. A 3.5-8 GHz Analog Complex Cross-Correlator for Interferometric Passive Millimeter-Wave Security Imaging Systems. In Proceedings of the 2018 Progress in Electromagnetics Research Symposium (PIERS-Toyama), Toyama, Japan, 1–4 August 2018; pp. 692–699.
46. Wang, C.; Xin, X.; Liang, B.; Li, Z.; Miao, J. Quadrature Errors and DC Offsets Calibration of Analog Complex Cross-Correlator for Interferometric Passive Millimeter-Wave Imaging Applications. *Sensors* **2018**, *24*, 677. [[CrossRef](#)]
47. Zhao, Y.; Hu, A.; Si, W.; Guo, X.; Miao, J. Calibration of Visibility Samples for Real-Time Passive Millimeter Wave Imaging. *IEEE Access* **2021**, *9*, 106441–106450. [[CrossRef](#)]
48. Thompson, A.R.; D’Addario, L.R. Frequency response of a synthesis array: Performance limitations and design tolerances. *Radio Sci.* **1982**, *17*, 357–369. [[CrossRef](#)]
49. Dilshad, U.; Chen, C.; Altaf, A.; Miao, J. An Ultra-Broadband K/Ka-Band (17-40 GHz) LNA MMIC in 0.15 μ m GaAs pHEMT. In Proceedings of the International Conference on Microwave and Millimeter Wave Technology (ICMMT), Guangzhou, China, 19–22 May 2019; pp. 1–3.
50. Carneiro, M.L.; Le Roy, M.; Pál’rennec, A.; Lababidi, R.; Ferrari, P.; Puyal, V. Compact Analog All-Pass Phase-Shifter in 65-nm CMOS for 24/28 GHz on-Chip- and in-Package Phased-Array Antenna. In Proceedings of the IEEE 23rd Workshop on Signal and Power Integrity (SPI), Chambéry, France, 18–21 June 2019; pp. 1–4.
51. Medina-Rull, A.; Pasadas, F.; Marin, E.G.; Toral-Lopez, A.; Cuesta, J.; Godoy, A.; Jimenez, D.; Ruiz, F.G. A Graphene Field-Effect Transistor Based Analogue Phase Shifter for High-Frequency Applications. *IEEE Access* **2020**, *8*, 209055–209063. [[CrossRef](#)]
52. Wu, P.-S.; Chang, H.-Y.; Tsai, M.-D.; Huang, T.-W.; Wang, H. New miniature 15–20-GHz continuous-phase/amplitude control MMICs using 0.18- μ m CMOS technology. *IEEE Trans. Microw. Theory Tech.* **2006**, *54*, 10–19.
53. Ellinger, F.; Jackel, H.; Bachtold, W. Varactor-loaded transmission-line phase shifter at C-band using lumped elements. *IEEE Trans. Microw. Theory Tech.* **2003**, *51*, 1135–1140. [[CrossRef](#)]
54. Wu, J.-C.; Kao, J.-C.; Kuo, J.-J.; Kao, K.-Y.; Lin, K.-Y. A 60-GHz single-ended-to-differential vector sum phase shifter in CMOS for phased-array receiver. In Proceedings of the 2011 IEEE MTT-S International Microwave Symposium, Baltimore, MD, USA, 5–10 June 2011; pp. 1–4.
55. Akbar, F.; Mortazawi, A. A New Integrated K-Band Analog Vector Sum Phase Shifter. In Proceedings of the IEEE/MTT-S International Microwave Symposium—IMS, Philadelphia, PA, USA, 10–15 June 2018; pp. 1441–1444.